Mechanism and Machine Theory 149 (2020) 103807

Contents lists available at ScienceDirect

Mechanism and Machine Theory

journal homepage: www.elsevier.com/locate/mechmachtheory

Research paper

Design and validation of a spatial two-limb 3R1T parallel manipulator with remote center-of-motion

Genliang Chen[a,b,*], Jue Wang[a,b], Hao Wang[a,b], Chao Chen[c], Vincenzo Parenti-Castelli[d], Jorge Angeles[e]

[a] State Key Laboratory of Mechanical Systems and Vibration, Shanghai Jiao Tong University, Shanghai 200240, China
[b] Shanghai Key Laboratory of Digital Manufacturing for Thin-Walled Structures, Shanghai Jiao Tong University, Shanghai 200240, China
[c] Department of Mechanical and Aerospace Engineering, Monash University, Clayton, Victoria 3802, Australia
[d] Department of Mechanical Engineering, University of Bologna, Bologna 40136, Italy
[e] Department of Mechanical Engineering and Center for Intelligent Machines, McGill University, Montreal, QC H3A 0C3, Canada

ARTICLE INFO

Article history:
Received 17 November 2019
Revised 5 January 2020
Accepted 20 January 2020
Available online 12 February 2020

Keywords:
Parallel manipulator
Remote center-of-motion
Virtual screw
Minimally invasive surgery

ABSTRACT

Remote center-of-motion (RCM) manipulators play an important role in minimally invasive surgery (MIS), which reduces the risk of infection, with less pain and fast recovery. In this paper, a novel spatial two-limb parallel manipulator, with 3R1T motion capabilities, supplied with a RCM, is synthesized for applications in MIS. The proposed manipulator consists of two identical limbs with a URRH chain, in which fully decoupled parallel wrists are employed to actuate the universal joints. Moreover, a cable-driven mechanism is introduced to produce the translational and rotational motions of the end-effector about its central shaft. Because of this particular design, the synthesized RCM manipulator possesses a compact structure and is partially decoupled in kinematics, which eases the implementation and simplifies its control. In order to validate the feasibility of the proposed idea, a prototype of the synthesized RCM manipulator is developed and experiments are conducted. The results show that the four dof prototype exhibits acceptable 3R1T RCM characteristics and positioning accuracy, by virtue of the adopted fabrication procedures. Thus, the synthesized manipulator offers potential applications in MIS.

1. Introduction

Robot-assisted minimally invasive surgery (RAMIS) has been increasingly adopted in a wide range of therapeutical procedures, such as endoscopy-assisted neurosurgery [1], intraocular operations [2], and magnetic resonance imaging-guided prostate interventions [3], because of its tremendous advantages over the traditional invasive procedures. In this kind of surgical systems, remote center-of-motion manipulators, which mechanically allow their end-effector to achieve large amplitude motions through a stationary point distant from the fixed base-frame [4], plays a key role in performing complex operations through small incisions. Therefore, more and more attention has been assigned to the synthesis and the implementation of novel RCM manipulators with dexterous mobility and compact structure. A variety of mechanisms with RCM characteristics have been proposed over the past decades.

In the existing RAMIS systems, including the well-known da Vinci surgical system [5], the planar double parallelogram mechanism, which was first proposed by Hamlin et al. [6] in 1994 and further developed by Taylor et al. [7,8], has been

* Corresponding author at: State Key Laboratory of Mechanical Systems and Vibration, Shanghai Jiao Tong University, Shanghai 200240, China.
E-mail address: leungchan@sjtu.edu.cn (G. Chen).

https://doi.org/10.1016/j.mechmachtheory.2020.103807
0094-114X/

widely adopted to realize the RCM characteristics. Based on this linkage, a variety of related RCM mechanisms have been proposed during the past decade. By introducing the concept of virtual parallelogram, Wang et al. [9,10] proposed a class of two degree-of-freedom (DOF) planar RCM mechanisms for MIS. Similarly, Zhang et al. [11] reported the type synthesis of a new family of RCM mechanisms upon generating the double parallelogram linkage into N-parallelograms. Based on this idea, Gijbels et al. [12] and Nisar et al. [13] also proposed a variety of planar 2-DOF RCM mechanism capable of providing pitch and translation. Inspired by the Peaucellier-Lipkin straight-line mechanism, Chen et al. [14] proposed a new type of planar 2-DOF RCM mechanisms by docking two parallelogram limbs in parallel. In addition, by arranging two parallelogram-based limbs in an orthogonal array, Clavel et al. [15] and Kuo et al. [16] proposed their RCM designs with two rotational (yaw and pitch) dof. Using timing belt and pulley as motion constraints, Patel et al. [17] proposed a similar two-limb four dof parallel RCM mechanism by means of an extra translational and rolling motion on the end-effector.

In addition to these parallelogram-based architectures, many alternative solutions have also been reported for the synthesis of RCM mechanisms. Based on the concept of virtual center linkages, Zong et al. [18] developed a systematic approach for the type synthesis of one dof RCM mechanisms. Jin et al. [19] proposed a new type synthesis method for RCM mechanisms based on the coupled motion of two virtual center-of-motion (VCM) linkages. Using tracking arcs, Hempel et al. [20] also proposed a compact RCM mechanism for magnetic resonance imaging-guided radiological interventions. By introducing the dual-triangular linkage, Chen and coworkers [21,22] developed a novel one dof RCM mechanism, which significantly reduces the space requirements.

Apart from the usage of special closed-loop linkages, many mechanisms with a fully parallel structure have been employed for the synthesis of spatial RCM manipulators. Wang et al. [23] proposed a family of spatial fully parallel mechanisms with RCM characteristics generated by intersecting motion planes. The four dof RAVEN robot [24], in which the RCM characteristics is guaranteed by a serial spherical limb and actuated by two extra UPS limbs, was developed as a telesurgical system for MIS. Here, U, P, and S stand for the universal, prismatic and spherical joints, respectively. The underlined 'P' indicates, in turn, that the prismatic joint is active. By taking advantage of spherical mechanisms, Kuo and Dai [25] proposed a novel four dof parallel RCM mechanism with fully-decoupled end-effector motion. Clavel et al. [26] developed a compact spatial parallel RCM manipulator with three rotations and one translation, whose end-effector is externally positioned for the sake of space economy. Based on the ingenious structure of the 'Agile Eye', Gosselin et al. [27] proposed a novel class of four-legged parallel mechanisms with 3R1T RCM motion type. Li et al. [28] submitted a comprehensive study on the type synthesis of SP-equivalent motion generators. A special family of 3R1T parallel RCM mechanisms with fixed linear actuators has been proposed as potential candidates for RAMIS systems.

Among the existing RCM mechanisms, many of them have less than four dof, such that additional actuators mounted on the manipulator end-effector are required to accomplish the 3R1T RCM requirement [29], namely concurrent pan-tilt-spin and axis translation. As a consequence, the structure of these manipulators [15–17,20,24–26] becomes complex and the inertia of the moving bodies increases in order to keep them stiff enough to carry the heavy actuators. Although several fully parallel four dof RCM manipulators [27,28] have been synthesized with all actuators fixed on the base platform, their four-limb structure makes them significantly space-consuming which greatly restricts their practicality. Moreover, all those manipulators are over-constrained, which requires high-precision fabrication.

On the basis of the above considerations, this paper proposes the synthesis of a novel spatial 3R1T RCM mechanism with a fully parallel structure. In general, four dof motion such as Schönflies motion (3T1R) calls for four limbs [30]. However, as mentioned above, a four-limb structure limits the workspace as well as being unsuitable for application to MIS, as the end-effector cannot be externally positioned. Thus, the design of this new RCM manipulator is inspired by the ingenious Schönflies motion (3T1R) generator by Harada and Angeles [31]. As shown in Fig. 1, the proposed four dof RCM manipulator consists of two identical limbs with the URRH- structure. Here, 'R' and 'H' stand for revolute and helical joints, respectively. The active 'U' joint is actuated by a decoupled 2-DOF parallel wrist fixed on the base platform. On the distal end, the concept of virtual screw is adopted the axial rotation (rolling) and translation (insertion) via a cable-driven differential motion mechanism. Because of the above particular design, the proposed 3R1T parallel RCM manipulator has a compact structure with all actuators fixedly mounted on the stationary base, which can significantly reduce the inertia of moving bodies. Moreover, the end-effector motion of the proposed RCM manipulator is partially decoupled, which simplifies the control. In order to validate the feasibility of the synthesized manipulator, a prototype is developed and preliminary experiments have been conducted. The results show that the 4-DOF prototype exhibits acceptable 3R1T RCM characteristics, as well as positioning accuracy, in light of the adopted fabrication techniques.

This paper is organized as follows: In Section 2, the conceptual design of the proposed two-limb 3R1T parallel RCM manipulator is introduced. Details of the developed prototype are given in Section 3. Closed-form solutions to both the forward and the inverse kinematics, as well as the Jacobian matrix, are derived in Section 4. Preliminary experiments are reported in Section 5 to validate the feasibility of the synthesized RCM manipulator. Conclusions are included in Section 6.

2. Preliminary design of 3R1T parallel RCM manipulator

This section presents the conceptual design of the proposed two-limb spatial 3R1T parallel RCM mechanism. A variety of planar limb structures are enumerated as alternatives for the synthesis of 4-DOF RCM mechanisms. In addition, the RCM feature of the synthesized mechanism is rigorously proved via the pattern analysis of the transformation matrix.

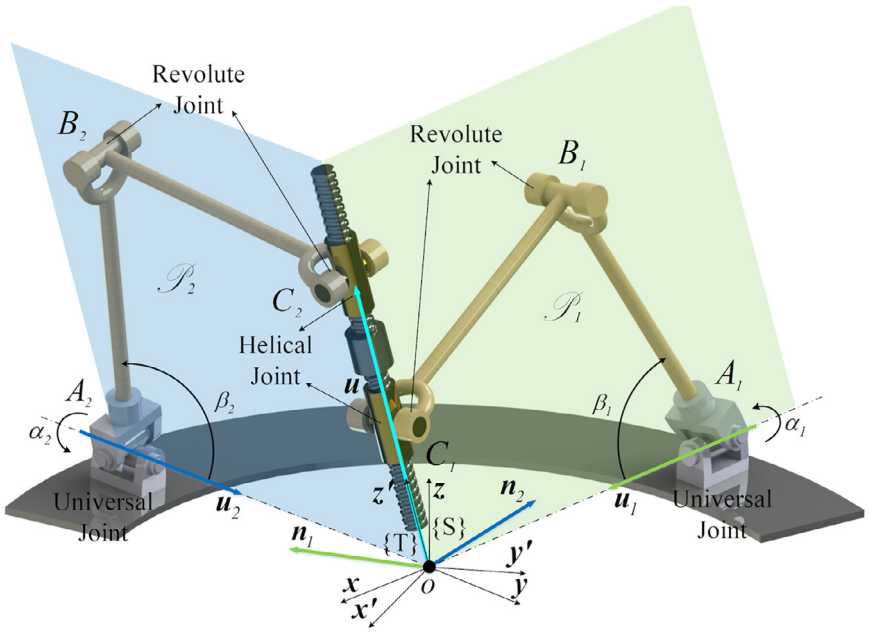

Fig. 1. Schematic of the proposed two-limb spatial 3R1T parallel RCM mechanism.

2.1. Architecture of the spatial RCM mechanism

As shown in Fig. 1, the proposed parallel RCM mechanism is composed of two identical limbs with the URRH structure. Here, the ground-fixed universal joints are actuated, their two dof rotations being independently controlled by corresponding actuators, the others being passive.

In each limb, the second axis of the U-joint and the two R-joints are all normal to the same plane, which is labeled $\mathcal{P}_i$ in Fig. 1. Meanwhile, both the fixed axes of the U-joint and the distal H-joint lie within the limb plane, normal to the axes of the other two joints in the limb. As a consequence, the whole URRH limb is confined to $\mathcal{P}_i$ whose normal $\boldsymbol{n}_i$ can be determined according to the rotation of the fixed axis of the corresponding U-joint.

In the proposed mechanism, the fixed axes of the U-joints, parallel to the unit vectors $\boldsymbol{u}_1$ and $\boldsymbol{u}_2$, intersect at one common point, denoted O, as shown in Fig. 1. At the other end, the distal H-joints in the two limbs share the same helical axis, which serves as the end-effector of the parallel mechanism. Because these H-joints are confined to their own limb planes, their common screw axis simply corresponds to the intersection of $\mathcal{P}_1$ and $\mathcal{P}_2$, denoted $\mathcal{L}_0$, which can be readily identified from a geometric point of view. Since this intersection line belongs to the two limb planes, it should pass through O and point in a direction normal to $\boldsymbol{n}_1$ and $\boldsymbol{n}_2$, donoted by the unit vector $\boldsymbol{u}$. Therefore, the direction of the end-effector can be uniquely determined according to the rotations of the U-joint fixed axes. On the other hand, the end-effector of the mechanism is connected to the kinematic limbs via two coaxial helical joints, so that the axial rotation and translation about its central shaft can be realized by the differential motion generated within the two planar limbs.

From the above discussion, it is apparent that the synthesized two-limb parallel mechanism is capable of spatial RCM functions about the stationary point O. More precisely, the mechanism offers three rotational and one translational dof with its end-effector always passing through the point O. The synthesis of this RCM mechanism is inspired by the 3T1R Schönflies-motion generator 2-CRRH, proposed by Lee et al. [32] and prototyped by Angeles and Harada's [31], for fast pick-and-place tasks. In this paper, the cylindrical drives are replaced by fully actuated U-joints. Thus, the motion of the planar limbs can be changed from translation along a specific direction to the rotation about a fixed axis. As a result, 3R1T mobility with RCM features can be generated by the proposed mechanism.

2.2. Variation of the spatial parallel RCM manipulator

As indicated above, the proposed 3R1T parallel RCM manipulator is realized by two planar limbs. On the proximal ends, these two-limb planes can be actively pivoted about two concurrent axes, namely $\boldsymbol{u}_1$ and $\boldsymbol{u}_2$. As well, on their distal ends, the limbs are coupled to the end-effector through two coaxial helical joints with distinct pitches.

According to its particular structure, the mobility of the synthesized 3R1T parallel RCM mechanism can be decomposed into two parts. On one hand, the direction of the end-effector central shaft, namely the axis of the coupled H-joints, can be uniquely determined according to the orientation of the limb planes. On the other hand, the axial translation and rotation

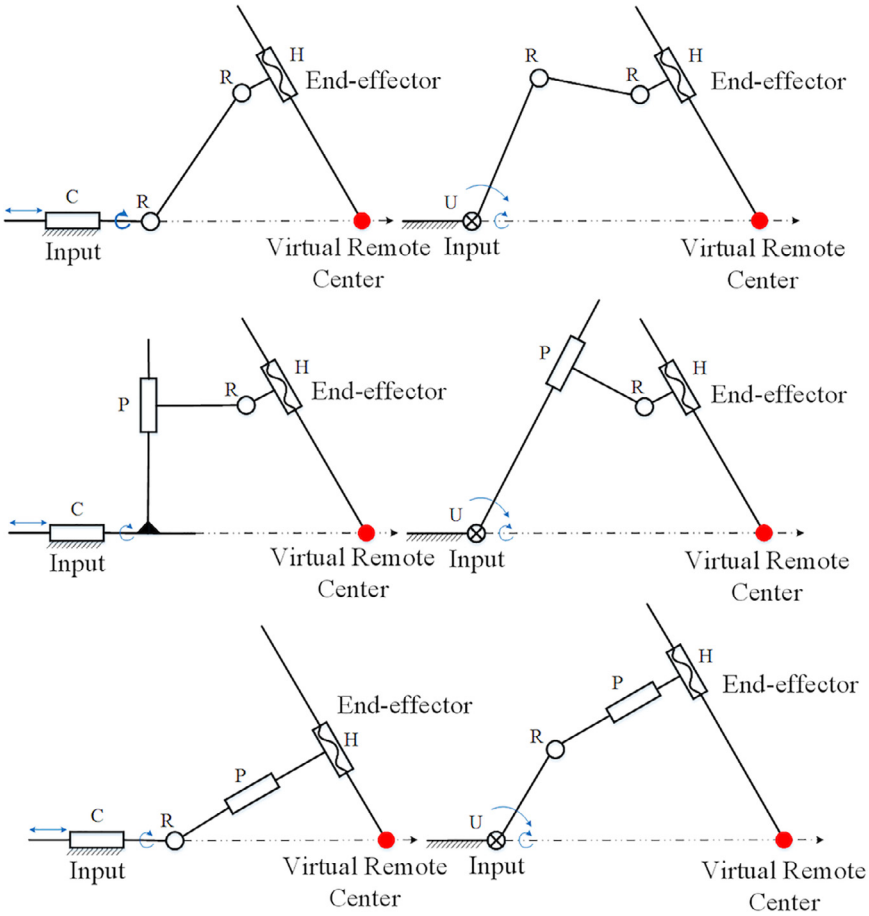

Fig. 2. Variation of the potential structures of planar limbs.

about the central shaft are achieved by means of the differential motion of the coupled H-joints that are driven through planar 4-bar linkages within the limbs.

As a matter of fact, there are a number of alternative four-bar linkages that can be utilized as candidate limb structures for the synthesis of the parallel RCM mechanism. As illustrated in Fig. 2, either a revolute or a translational joint can be employed to actuate the distal H-joint through the planar four-bar linkage. Accordingly, an active U or C joint will be generated as the two dof driver to actuate the planar limbs. For each case, three dyads, PR, RR, and RP as illustrated in the figure, can be used as candidates to transfer the motion of the limbs' two dof actuators to the end-effector of the manipulator. Hence, any combination of the above two dof actuator (U or C) and a dyad link (PR, RR, or RP) can be introduced as available planar limbs for the synthesis of the desired spatial parallel RCM mechanism. Meanwhile, there are also a couple of alternative ways to realize the differential motion about the axis of the coupled dual H-joints shown in the Fig. 6

2.3. Preliminary design

In this paper, two URRH limbs are selected to construct the 3R1T parallel RCM mechanism, based on which a prototype has been developed and tested to verify the feasibility of the proposed synthesis approach. The reasons behind the choice of this architecture are given below.

(1). As shown in the Fig. 3, we made an active 2-DOF cylindrical driver proposed by Karimi Eskandary and Angeles [33]. Compared with the universal joint shown in the Fig. 5, the actuated cylincal joint needs a relatively long slider which requires more space. As a consequence, it is not easy to achieve a compact structure using C drives.

(2). The reason why we choose the RR dyads as a passive joint is that a passive P joint is much harder to design and manufacture than its R counterpart. Besides, the force transmission characteristic of the RR link is better than PR and RP alternatives, for friction and pressure angle of the P joint need be considered. In addition, the structure of the passive R joint can be more compact, besides entailing a smaller manufacturing error.

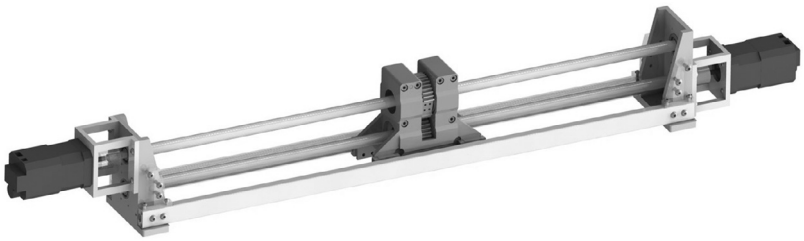

Fig. 3. Schematic of the 2-DOF active C-drive.

2.4. Mobility analysis via the pattern of transform matrix

In this section, the method of *Pattern of Transform Matrix* [34] is introduced to characterize the mobility of the synthesized spatial parallel mechanism. Both the dof and the RCM feature of the proposed two-limb parallel manipulator can be found rigorously via this method.

As shown in Fig. 1, a spatial frame {S} fixed to the base is constructed at the intersection of the axes of the two U-joints, namely *O*. The corresponding $\boldsymbol{x}$ and $\boldsymbol{y}$ axes are set to be coincident with $\boldsymbol{u}_1$ and $\boldsymbol{u}_2$ counterparts, respectively. It should be noted that, for simplicity of the presentation but without loss of generality, it is assumed that the $\boldsymbol{u}_1$ and $\boldsymbol{u}_2$ axes are perpendicular to each other. Further, in the home configuration, both the limb planes $\mathcal{P}_1$ and $\mathcal{P}_2$ are perpendicularly intersecting the $\boldsymbol{z}$ axis. Meanwhile, the tip frame {T} is attached to the manipulator end-effector, which is initially coincident with {S} in the home configuration.

Using the pattern analysis approach [34], the kinematics of the URRH~ limbs in the synthesized parallel manipulator can be represented as a serial combination of three motions: the rotation about the fixed axis of the U-joint, the planar motion within the limb plane, and the helical motion about the central shaft. Then, in light of limb 1, the relative pose of {T} with respect to {S} can be expressed via a homogeneous transformation matrix as

$$\mathbf{g}_{st,1}(\alpha_1, \beta_1, x_1, z_1, \gamma_1) = \mathrm{R}(\boldsymbol{x})\mathrm{G}(\boldsymbol{y})\mathrm{H}(\boldsymbol{z}, h_1) = \begin{bmatrix} \mathbf{R}_1 & \boldsymbol{p}_1 \\ \boldsymbol{0}_3^T & 1 \end{bmatrix} \tag{1}$$

where $\mathbf{R}(\alpha_1)$, $\mathbf{G}(\beta_1, x_1, z_1)$, and $\mathbf{H}(\gamma_1)$ denote the rotation about the $\boldsymbol{x}$ axis, the planar motion within $\mathcal{P}_1$ and the helical motion about the $\boldsymbol{z}$-axis of pitch h_1, respectively. $\{\alpha_1\}$, $\{\beta_1, x_1, z_1\}$, and γ_1 are the corresponding variables of the motions. More details are available in the literature [34].

In Eq. (1), $\mathbf{R}_1 \in SO(3)$ and $\boldsymbol{p}_1 \in \mathbb{R}^{3\times 1}$ represent the orientation of a rigid body and the position of one of its points, respectively, which can be expanded as

$$\begin{cases} \mathbf{R}_1 = \begin{bmatrix} f_{11}(\alpha_1, \beta_1, \gamma_1) & f_{12}(\alpha_1, \beta_1, \gamma_1) & f_{13}(\alpha_1, \beta_1, \gamma_1) \\ f_{21}(\alpha_1, \beta_1, \gamma_1) & f_{22}(\alpha_1, \beta_1, \gamma_1) & f_{23}(\alpha_1, \beta_1, \gamma_1) \\ f_{31}(\alpha_1, \beta_1, \gamma_1) & f_{32}(\alpha_1, \beta_1, \gamma_1) & f_{33}(\alpha_1, \beta_1, \gamma_1) \end{bmatrix} \\ \boldsymbol{p}_1 = \begin{bmatrix} f_{14}(\beta_1, x_1, \gamma_1) \\ f_{24}(\alpha_1, \beta_1, z_1, \gamma_1) \\ f_{34}(\alpha_1, \beta_1, z_1, \gamma_1) \end{bmatrix} = \begin{bmatrix} x_1 + h_1\gamma_1 S_{\beta_1} \\ -z_1 S_{\alpha_1} - h_1\gamma_1 S_{\alpha_1} C_{\beta_1} \\ z_1 C_{\alpha_1} + h_1\gamma_1 C_{\alpha_1} C_{\beta_1} \end{bmatrix} \end{cases}$$

where the entries of $\mathbf{R}_1$ can be readily obtained as the composition of two motion subgroups. Here, $C_{(x)} = \cos(x)$ and $S_{(x)} = \sin(x)$ for simplicity.

Analogously, in limb 2, the relative pose of {T} with respect to {S} can be represented as

$$\mathbf{g}_{st,2}(\alpha_2, \beta_2, y_2, z_2, \gamma_2) = \mathrm{R}(\boldsymbol{y})\mathrm{G}(\boldsymbol{x})\mathrm{H}(\boldsymbol{z}, h_2) = \begin{bmatrix} \mathbf{R}_2 & \boldsymbol{p}_2 \\ \boldsymbol{0}_3^T & 1 \end{bmatrix} \tag{2}$$

where the variables are defined in the same way as those in (1). While the orientation and position components can be given by

$$\begin{cases} \mathbf{R}_2 = \begin{bmatrix} f'_{11}(\alpha_2, \beta_2, \gamma_2) & f'_{12}(\alpha_2, \beta_2, \gamma_2) & f'_{13}(\alpha_2, \beta_2, \gamma_2) \\ f'_{21}(\alpha_2, \beta_2, \gamma_2) & f'_{22}(\alpha_2, \beta_2, \gamma_2) & f'_{23}(\alpha_2, \beta_2, \gamma_2) \\ f'_{31}(\alpha_2, \beta_2, \gamma_2) & f'_{32}(\alpha_2, \beta_2, \gamma_2) & f'_{33}(\alpha_2, \beta_2, \gamma_2) \end{bmatrix} \\ \boldsymbol{p}_2 = \begin{bmatrix} f'_{14}(\alpha_2, \beta_2, z_2, \gamma_2) \\ f'_{24}(\beta_2, z_2, \gamma_2) \\ f'_{34}(\alpha_2, \beta_2, z_2, \gamma_2) \end{bmatrix} = \begin{bmatrix} z_2 S_{\alpha_2} + h_2\gamma_2 S_{\alpha_2} C_{\beta_2} \\ y_2 - h_2\gamma_2 S_{\beta_2} \\ z_2 C_{\alpha_2} + h_2\gamma_2 C_{\alpha_2} C_{\beta_2} \end{bmatrix} \end{cases}$$

Since the fixed base and the moving end-effector are common to the two limbs of the parallel manipulator, the closure of the kinematic chain leads to

$$\mathbf{g}_{st,1} = \mathbf{g}_{st,2} \Rightarrow \begin{cases} \mathbf{R}_1 = \mathbf{R}_2 \\ \boldsymbol{p}_1 = \boldsymbol{p}_2 \end{cases} \tag{3}$$

In the closure Eq. (3), six independent constraints (three on the orientations $\mathbf{R}_i$, $i = 1, 2$ and the other three on the positions $\boldsymbol{p}_i$) are dericed from the transformation matrices $\mathbf{g}_{st,i}$. Note six constraints are derived out of 10 variables between the two limbs. As a result, the synthesized manipulator has four dof.

Further, from the pattern of the orientation matrices, there are three independent variables out of the total six, $\{\alpha_1, \beta_1, \gamma_1\}$ and $\{\alpha_2, \beta_2, \gamma_2\}$, according to the constraints. This implies that the synthesized two-limb parallel manipulator has three rotational dof. In other words, the end-effector of the manipulator can be arbitrarily oriented in terms of three independent variables. Once the orientation of the manipulator's end-effector is determined, there is only one independent variable left to specify the corresponding position. Therefore, it can be stated that the proposed 2-URRH parallel manipulator has 3 rotational and 1 translational (3R1T) dof.

Given the end-effector orientation, namely both $\{\alpha_1, \beta_1, \gamma_1\}$ and $\{\alpha_2, \beta_2, \gamma_2\}$, the position vectors $\boldsymbol{p}_1$ and $\boldsymbol{p}_2$ relate to two planes that can be represented in a compact form as

$$\begin{cases} \boldsymbol{p}_1 \rightarrow \; y + \frac{S_{\alpha_1}}{C_{\alpha_1}} z = 0 \\ \boldsymbol{p}_2 \rightarrow \; x - \frac{S_{\alpha_2}}{C_{\alpha_2}} z = 0 \end{cases} \tag{4}$$

where the intersection is readily obtained in the form

$$\boldsymbol{p} = \boldsymbol{p}_0 + \lambda \boldsymbol{u} \Rightarrow \boldsymbol{p}_0 = \begin{bmatrix} x_0 \\ y_0 \\ z_0 \end{bmatrix}, \; \boldsymbol{u} = \begin{bmatrix} -C_{\alpha_1} S_{\alpha_2} \\ S_{\alpha_1} C_{\alpha_2} \\ -C_{\alpha_1} C_{\alpha_2} \end{bmatrix} \tag{5}$$

where $\boldsymbol{p}_0 = \boldsymbol{0}_{3\times 1}$ is a particular solution to the two plan Eq. (4), which relates to a stationary point on the intersection line. $\boldsymbol{u}$ being a vector associated with the line direction.

Moreover, it can be readily proven that vector $\boldsymbol{u}$ is proportional to the third columns of $\mathbf{R}_1$ and $\mathbf{R}_2$, which correspond to the direction of the central shaft of the end-effector. This indicates that once the orientation of the end-effector is specified, the manipulated object can only translate along its central shaft. Note that $\boldsymbol{p}_0$ is constant and independent of all motion variables. The central shaft always passes through the origin of {S}, namely *O*, when its orientation and axis position change during the tasks. As well, this intrinsic property of the motion understudy meets exactly the fundamental requirements for mechanisms performing RCM manipulation.

3. Prototyping of the spatial RCM manipulator

This section discusses the prototyping of the proposed 3R1T parallel RCM mechanism with the URRH-HRRU structure, as illustrated in Fig. 4. In the prototype, a decoupled two-DOF parallel wrist [35] is introduced for each limb as the active U-joint to be driven by two servo motors mounted on the fixed base. On the other hand, the concept of virtual screw [36] is employed to generate the axial rotation and translation of the central shaft on the manipulator end-effector through a compact tendon-driven mechanism.

3.1. Design of a decoupled two-DOF parallel wrist

Inspired by the decoupled two dof parallel wrist proposed by Carricato and Parenti-Castelli [35], a compact U driver is proposed to actuate the planar limbs of the synthesized parallel RCM mechanism. As shown in Fig. 5, the fixed axis of the U-joint is directly actuated by a DC motor via the Capstan cable-drive system. A tensioner is integrated to prevent the tendon from slipping about the DC motor output shaft and reduce the backlash between the roll-roll capstan wheels. Moreover, an arbitrary transmission ratio can be achieved for this particular cable-driven system upon adjusting the radii of the two wheels.

On the other hand, the rotation of the U-joint second axis is realized through a planar slider-crank linkage is driven by another DC motor through a rail-guided ball screw actuator mounted on the fixed base. A key issue in this design is the addition of a passive R-joint, which is coaxial with the fixed shaft of the U-joint, attached to the slider. Thus, the whole plane of the slider-crank linkage can passively pivot about the fixed shaft to accommodate the limb orientation to the rotation of the U-joint first axis. The main advantage of such a design relies on the decoupling of the two rotations of the active U-joint. Hence, the two axes of the U-joint can be independently actuated by two servo motors mounted on the fixed base. This leads to the compactness of the two dof U actuator to reduce the mass of the moving parts in the planar limbs. Further, the control scheme of the synthesized parallel RCM manipulator can be simplified for its kinematics is partially decoupled, which will be intensively discussed in the section below.

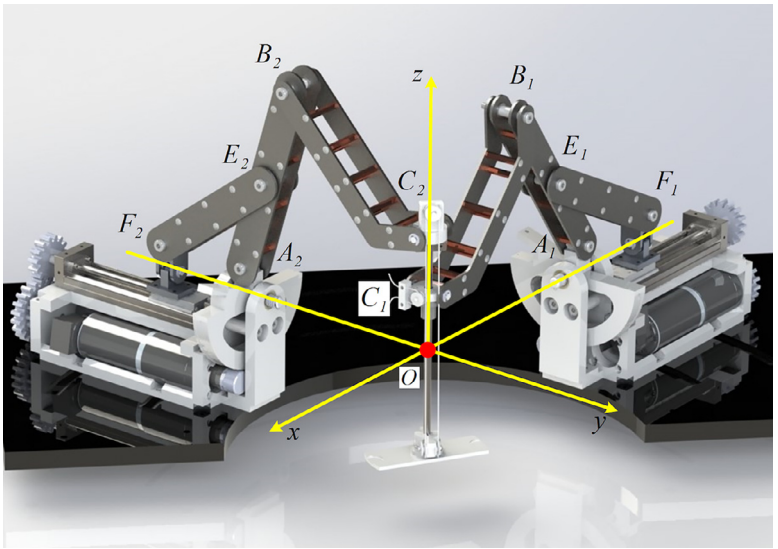

Fig. 4. CAD model of the 3R1T parallel RCM manipulator: URRH-HRRU.

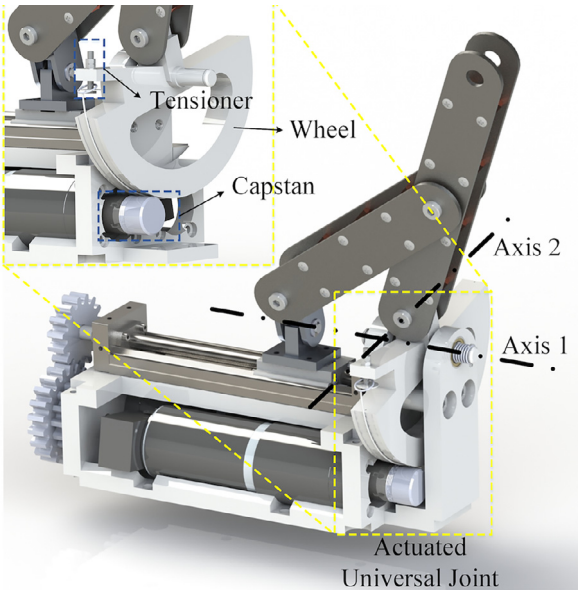

Fig. 5. Structure of the active U-joint in the limbs of the developed manipulator.

3.2. Realization of the dual helical joint via a virtual screw

As indicated in Section 2.1, a dual helical joint is employed to connect the two planar URRH limbs to the end-effector, as shown in Fig. 6. This compound joint serves as a differential motion device to generate axial translation and rotation about the central shaft of the manipulator end-effector. Once the direction of the end-effector is specified according to the rotation of the first axes of U-joints, the positions of the nuts along the central shaft can be regarded as the outputs of the crank-slider linkages on the corresponding limb planes, which are driven by the second axes of the U-joints. Then, pure translation of the end-effector can be achieved when the two nuts move in the same direction at the same rate. When they move at the same rate in the opposite directions, pure rotation about its central shaft is generated. Otherwise, the axial translation and rotation of the end-effector are coupled with each other.

In our prototype, the concept of virtual screw [36] was borrowed to replace the dual H-joint. As shown in Fig. 6, a tendon-driven mechanism is employed to transmit the translation of the collars to the axial translation and concomitant rotation of the end-effector cylindrical motion of its central shaft. The merit of such a cable-constraint version is the reduction of friction by using ball bearing pulleys. Moreover, the ratio between translation and rotation, namely the pitch of

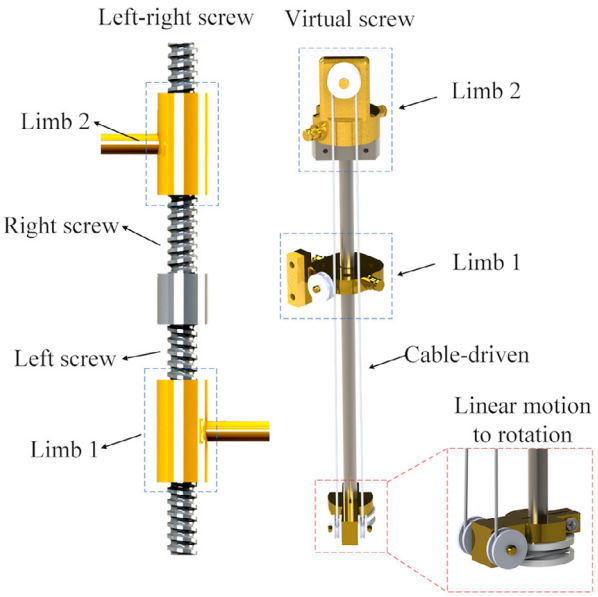

Fig. 6. Realization of the virtual screw with a cable-driven mechanism.

virtual screw, can be adjusted readily by changing the radius of the pulleys. In the developed prototype, the end-effector is attached to the collar of limb 2 via a revolute joint, to some extent, which can be regarded as a H-joint of 0 pitch. Thus, the axial position of the central shaft can be completely specified according to the motion of the U-joint second axis in the corresponding limb. The rotation is generated by the relative motion of collar 1 with respect to the counterpart in limb 2.

In the developed 3R1T parallel RCM manipulator, two sets of DC servo motors (Maxon RE40 150W) with gearheads and encoders are used to actuate the U-joint in each limb. Meanwhile, the CANopen interface is used to synchronously coordinate the motion of the servo motors via the commercial controllers (Maxon Epos2).

4. Kinematics modeling and analysis

In this section, the kinematics modeling and analysis (both the forward and the inverse problems) of the synthesized spatial parallel RCM manipulator is discussed. The Jacobian matrix of the manipulator is derived, the singularity analysis then following suit.

4.1. Forward kinematics

As indicated in Section 2, the forward kinematics modeling of the proposed manipulator can be accomplished through two steps. First, the direction of the central shaft can be uniquely specified according to the rotation of the U-joints about their fixed axes. Then, the URRH limbs degenerate into planar crank-slider four-bar linkages whose kinematics is available in closed-form. Thus, the axial translation and rotation of the end-effector is determined in light of differential motion between the dual H-joints along the central shaft.

Because of the particular structure of the synthesized manipulator, the central shaft of the end-effector is nothing but the intersection of the two limb planes, pivoted about two concurrent axes mounted on the fixed base. Thus, the unit vector associated with the intersection line can be obtained directly as

$$\boldsymbol{u} = \frac{\boldsymbol{n}_2 \times \boldsymbol{n}_1}{\|\boldsymbol{n}_2 \times \boldsymbol{n}_1\|} \tag{6}$$

where $\boldsymbol{n}_i = \exp(\hat{\mathbf{u}}_i \alpha_i)\boldsymbol{v}_i$, $i = 1, 2$ denotes the unit normal vector of the limb plane $\mathcal{P}_i$. In turn, $\boldsymbol{v}_i$ is the same vector in its home position, which lies in the ***xy***-plane and perpendicular to $\boldsymbol{u}_i$. The angular input of the corresponding U drive is represented α_i. Here, the matrix exponential $\exp(\hat{\mathbf{u}}_i \alpha_i) \in SO(3)$ is introduced to represent the rotation matrix about $\boldsymbol{u}_i$ by angle α_i in compact form. In turn, $\hat{\mathbf{u}}_i \in so(3)$ is the skew-symmetric matrix associated with $\boldsymbol{u}_i$, also known as the *cross-product matrix* of $\boldsymbol{u}_i$, usually represented as $\mathrm{CPM}(\boldsymbol{u}_i)$.

As indicated above, the fixed axes of the two active U-joints intersect each other in our prototype. Moreover, in the home configuration of the manipulator, both limb planes $\mathcal{P}_1$ and $\mathcal{P}_2$ remain vertical. Thus, $\boldsymbol{u}_1$, $\boldsymbol{u}_2$, and $\boldsymbol{u}_0$ define the coordinates frame {S}, with $\boldsymbol{v}_1 = \boldsymbol{u}_2$, $\boldsymbol{v}_2 = \boldsymbol{u}_1$.

As addressed in Section 3.1, in the prototype, a two dof parallel wrist is designed to actuate the U-joints in a decoupled way. Then, once the direction of the central shaft is specified, the limbs degenerate into planar six-bar linkages with double

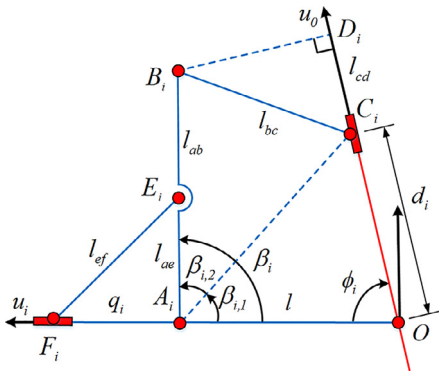

Fig. 7. Schematic of the planar linkage in the manipulator's limbs.

sliders. As shown in Fig. 7, the collar positions of the helical joints on the central shaft can be readily determined by means of the kinematics of six-bar linkages in light of the linear inputs of the active slider.

First, the position vector of the revolute joint B_i in {S} can be readily derived as

$$\boldsymbol{r}_{B_i} = \boldsymbol{r}_{A_i} + l_{ab}\exp(\hat{\mathbf{n}}_i\beta_i)\boldsymbol{u}_i \tag{7}$$

where $\boldsymbol{r}_{A_i} = -l_{oa}\boldsymbol{u}_i$ denotes the position vector of point A_i. β_i corresponds to the angle of rotation of the U-joint second axis, which can be determined according to the input of the active slider as

$$\beta_i = \pi - \arccos\frac{q_i^2 + l_{ae}^2 - l_{ef}^2}{2q_i l_{ae}}$$

where q_i denotes the length of A_iE_i considered as the input of the slider. Here, l_{oa}, l_{ab}, l_{ae}, and l_{ef} represent the lengths of the corresponding segments OA_i, A_iB_i, A_iE_i and E_iF_i, respectively.

Then, the collar position of the helical joint on the central shaft can be derived as

$$d_i = l_{od_i} = \boldsymbol{u}^T\boldsymbol{r}_{B_i} - \sqrt{l_{bc}^2 - \|(\mathbf{I} - \boldsymbol{u}\boldsymbol{u}^T)\boldsymbol{r}_{B_i}\|^2} \tag{8}$$

where $\boldsymbol{u}^T\boldsymbol{r}_{B_i}$ and $\|(\mathbf{I} - \boldsymbol{u}\boldsymbol{u}^T)\boldsymbol{r}_{B_i}\|$ correspond to the projective length and the normal distance of B_i from the central shaft of axis parallel vector $\boldsymbol{u}$, namely l_{od} and l_{bd}, respectively.

As a consequence, the axial translation and rotation of the end-effector's central shaft can be specified directly according to the kinematics of the cable-driven virtual screw in the light of the collar positions of the dual helical joints. Then, we have

$$\begin{cases} d = d_1 \\ \gamma = (d_1 - d_2)/p \end{cases} \tag{9}$$

where d_1 and d_2 are the positions of the dual H-joints, respectively, on the central shaft, given in Eq. (8). Here, p is the radius of the pulley, which can be regarded as the pitch of virtual screw.

4.2. Inverse kinematics

In the inverse kinematics problem, both the orientation and the axial position of the mechanism end-effector, namely $\boldsymbol{u}$ and $\{\gamma, d\}$, are given. Then, the rotation angles of the U-joint first axes can be determined directly as

$$\boldsymbol{u}^T(\exp(\hat{\mathbf{u}}_i\alpha_i)\boldsymbol{v}_i) = 0 \Rightarrow \alpha_i = \arccos\frac{\boldsymbol{v}_i^T(\boldsymbol{u}\times\boldsymbol{u}_i)}{\|\boldsymbol{u}\times\boldsymbol{u}_i\|} \tag{10}$$

where $\boldsymbol{n}_i = \boldsymbol{u}\times\boldsymbol{u}_i/||\boldsymbol{u}\times\boldsymbol{u}_i||$ points in the normal direction of $\mathcal{P}_i$.

Meanwhile, the positions of the dual H-joints on the central shaft can be specified according to Eq. (9) as

$$\begin{cases} d_1 = d \\ d_2 = d - p\gamma \end{cases} \tag{11}$$

As a result, the inputs of the linear sliders can be obtained by solving the inverse kinematics of the planar six-bar linkages within the limbs. First, the angle of rotation β_i can be derived as

$$\beta_i = \beta_{i,1} + \beta_{i,2} \tag{12}$$

where $\beta_{i,1}$ and $\beta_{i,2}$ are the internal angles of the two triangles defined in Fig. 7, given by

$$\begin{cases} \beta_{i,1} = \arccos \frac{l_{oa}^2 + \|\boldsymbol{r}_{C_i} - \boldsymbol{r}_{A_i}\|^2 - d_i^2}{2 l_{oa} \|\boldsymbol{r}_{C_i} - \boldsymbol{r}_{A_i}\|} \\ \beta_{i,2} = \arccos \frac{l_{ab}^2 + \|\boldsymbol{r}_{C_i} - \boldsymbol{r}_{A_i}\|^2 - l_{bc}^2}{2 l_{ab} \|\boldsymbol{r}_{C_i} - \boldsymbol{r}_{A_i}\|} \end{cases}$$

where the position vector $\boldsymbol{r}_{C_i} = d_i \boldsymbol{u}$.

The required input of the corresponding linear slider is specified as

$$q_i = -l_{ae} \cos \beta_i + \sqrt{l_{ef}^2 - l_{ae}^2 \sin^2 \beta_i} \tag{13}$$

From the above analysis, it is known that both the forward and inverse kinematics of the synthesized 3R1T parallel RCM manipulator can be obtained in closed-form. Therefore, the motion control of the manipulator can be readily implemented in an embedded commercial controller.

4.3. Jacobian matrix

In this section, the Jacobian matrix of the proposed manipulator is constructed using the concept of virtual chain [37]. The end-effector motion of the synthesized manipulator is equivalent to a serial 3R1T kinematic chain with RCM characteristics. Then, the forward kinematics of the equivalent chain can be represented using the product of exponential (POE) formula as

$$\mathbf{g}_{st}(\boldsymbol{\theta}) = \exp(\hat{\boldsymbol{\xi}}_1 \theta_1) \exp(\hat{\boldsymbol{\xi}}_2 \theta_2) \exp(\hat{\boldsymbol{\xi}}_3 \theta_3) \exp(\hat{\boldsymbol{\xi}}_4 \theta_4) \, \mathbf{g}_{st,0} \tag{14}$$

where $\hat{\boldsymbol{\xi}}_i \in se(3)$ $(i = 1, \cdots, 4)$ are the joint twists in the virtual kinematic chain of 3R1T RCM characteristics. As well, θ_i, $i = 1, \ldots, 4$ are the corresponding joint variables.

According to the kinematic characteristics, the joint twists in the virtual chain take the forms

$$\boldsymbol{\xi}_1 = \begin{bmatrix} \boldsymbol{u}_1 \\ \boldsymbol{0}_3 \end{bmatrix}, \ \boldsymbol{\xi}_2 = \begin{bmatrix} \boldsymbol{u}_2 \\ \boldsymbol{0}_3 \end{bmatrix}, \ \boldsymbol{\xi}_3 = \begin{bmatrix} \boldsymbol{0}_3 \\ \boldsymbol{u} \end{bmatrix}, \ \boldsymbol{\xi}_4 = \begin{bmatrix} \boldsymbol{u} \\ \boldsymbol{0}_3 \end{bmatrix} \tag{15}$$

which represent three rotations and one translation, the axes of rotation being concurrent at one fixed point.

The corresponding joint displacements can be represented concisely in the form

$$\begin{cases} \theta_1 = \alpha_1 - \alpha_{1,0} \\ \theta_2 = \phi_1 - \phi_{1,0} \\ \theta_3 = d - d_0 \\ \theta_4 = \gamma - \gamma_0 \end{cases} \tag{16}$$

where ϕ_1 corresponds to the angle between $\boldsymbol{u}$ and $\boldsymbol{u}_1$, as shown in Fig. 7, which yields $\phi_1 = \arccos(\boldsymbol{u}^T \boldsymbol{u}_1)$. Moreover, α_1, γ, and d were defined above. As well, $\alpha_{1,0}$, $\phi_{1,0}$, γ_0, and d_0 are their initial values in home configuration.

Then, the Jacobian matrix of the manipulator is derived as

$$(\dot{\mathbf{g}}_{st} \mathbf{g}_{st}^{-1})^{\vee} = \mathbf{J}_{\theta} \dot{\boldsymbol{\theta}} = \mathbf{J}_{\theta} \mathbf{J}_{\boldsymbol{q}} \dot{\boldsymbol{q}} \Rightarrow \mathbf{J} = \mathbf{J}_{\theta} \mathbf{J}_{\boldsymbol{q}} \tag{17}$$

where $\boldsymbol{q} = [\alpha_1, \alpha_2, \beta_1, \beta_2]^T$ is the vector array of the manipulator input variables. $\mathbf{J} \in \mathbb{R}^{6\times4}$ being the Jacobian matrix with columns given below:

$$\mathbf{J}_{\theta} = \left[\boldsymbol{\xi}_1', \boldsymbol{\xi}_2', \boldsymbol{\xi}_3', \boldsymbol{\xi}_4'\right] \in \mathbb{R}^{6\times4}, \ \mathbf{J}_{\boldsymbol{q}} = \frac{\partial \boldsymbol{\theta}}{\partial \boldsymbol{q}} \in \mathbb{R}^{4\times4} \tag{18}$$

where $\boldsymbol{\xi}_i' = \mathrm{Ad}\left(\exp(\hat{\boldsymbol{\xi}}_1 \theta_1) \cdots \exp(\hat{\boldsymbol{\xi}}_{i-1} \theta_{i-1})\right) \boldsymbol{\xi}_i \in \mathbb{R}^{6\times1}$ denote the joint twists in the current configuration of the manipulator, $\mathrm{Ad}(\exp(\hat{\boldsymbol{\xi}}_i \theta_i)) \in \mathbb{R}^{6\times6}$ being the adjoint representation of the exponential map.

According to the kinematics analysis, the intermediate factor $\mathbf{J}_{\boldsymbol{q}}$ can be derived in closed-form as

$$\mathbf{J}_{\boldsymbol{q}} = \frac{\partial \boldsymbol{\theta}}{\partial \boldsymbol{q}} = \begin{bmatrix} J_{11} & 0 & 0 & 0 \\ J_{21} & J_{22} & 0 & 0 \\ J_{31} & J_{32} & J_{33} & 0 \\ J_{41} & J_{42} & J_{43} & J_{44} \end{bmatrix}_{4\times4}$$

where the entries $\mathbf{J}_{ij} = \partial \theta_i / \partial q_j$ correspond to the partial derivatives, given by

$$\begin{cases} J_{11} = 1, \ J_{21} = a_{01} a_{11}, \ J_{22} = a_{01} a_{12} \\ J_{31} = a_{21} a_{11} + a_{31} a_{41}, \ J_{32} = a_{21} a_{12}, \ J_{33} = a_{31} a_{43} \\ J_{41} = \frac{1}{p}((a_{21} - a_{22}) a_{11} + a_{31} a_{41}), \ J_{43} = \ \ a_{31} a_{43}/p \\ J_{42} = \frac{1}{p}((a_{21} - a_{22}) a_{12} - a_{32} a_{42}), \ J_{44} = -a_{32} a_{44}/p \end{cases}$$

where the coefficients are given by

$$a_{01} = \frac{\partial \phi_1}{\partial \boldsymbol{u}} = -\frac{\boldsymbol{u}_1^T}{\sin\phi_1}$$

$$a_{11} = \frac{\partial \boldsymbol{u}}{\partial \alpha_1} = \frac{(\mathbf{I} - \boldsymbol{u}\boldsymbol{u}^T)\,\hat{\mathbf{n}}_2\hat{\mathbf{n}}_1\boldsymbol{u}_1}{\|\boldsymbol{n}_2 \times \boldsymbol{n}_1\|},\ a_{12} = \frac{\partial \boldsymbol{u}}{\partial \alpha_2} = \frac{(\mathbf{I} - \boldsymbol{u}\boldsymbol{u}^T)\,\hat{\mathbf{n}}_1\hat{\mathbf{n}}_2\boldsymbol{u}_2}{\|\boldsymbol{n}_2 \times \boldsymbol{n}_1\|}$$

$$a_{21} = \frac{\partial d_1}{\partial \boldsymbol{u}} = \left(1 - \frac{\boldsymbol{u}^T\boldsymbol{r}_{B_1}}{l_{cd,1}}\right)\boldsymbol{r}_{B_1},\ a_{22} = \frac{\partial d_2}{\partial \boldsymbol{u}} = \left(1 - \frac{\boldsymbol{u}^T\boldsymbol{r}_{B_2}}{l_{cd,2}}\right)\boldsymbol{r}_{B_2}$$

$$a_{31} = \frac{\partial d_1}{\partial \boldsymbol{r}_{B_1}} = \left(1 - \frac{\boldsymbol{u}^T\boldsymbol{r}_{B_1}}{l_{cd,1}}\right)\boldsymbol{u} + \frac{\boldsymbol{r}_{B_1}}{l_{cd,1}},\ a_{32} = \frac{\partial d_2}{\partial \boldsymbol{r}_{B_2}} = \left(1 - \frac{\boldsymbol{u}^T\boldsymbol{r}_{B_2}}{l_{cd,2}}\right)\boldsymbol{u} + \frac{\boldsymbol{r}_{B_2}}{l_{cd,2}}$$

$$a_{41} = \frac{\partial \boldsymbol{r}_{B_1}}{\partial \alpha_1} = \hat{\mathbf{u}}_1(\boldsymbol{r}_{B_1} - \boldsymbol{r}_{A_1}),\ a_{43} = \frac{\partial \boldsymbol{r}_{B_1}}{\partial \beta_1} = \hat{\mathbf{n}}_1(\boldsymbol{r}_{B_1} - \boldsymbol{r}_{A_1})$$

$$a_{42} = \frac{\partial \boldsymbol{r}_{B_2}}{\partial \alpha_2} = \hat{\mathbf{u}}_2(\boldsymbol{r}_{B_2} - \boldsymbol{r}_{A_2}),\ a_{44} = \frac{\partial \boldsymbol{r}_{B_2}}{\partial \beta_2} = \hat{\mathbf{n}}_2(\boldsymbol{r}_{B_2} - \boldsymbol{r}_{A_2})$$

where $l_{cd,i} = (l_{bc}^2 - \|(\mathbf{I} - \boldsymbol{u}\boldsymbol{u}^T)\boldsymbol{r}_{B_i}\|^2)^{\frac{1}{2}}$.

Using the proposed method, the closed-form expression of the Jacobian matrix of the manipulator can be derived as a product of two factors. The first relates to the joint twists of the virtual RCM kinematic chain in the current configuration of the manipulator. The second corresponds to the transmission rate from the U-joints to the virtual ones. Then, a Jacobian-based analysis can be readily implemented for the synthesized manipulator.

4.4. Singularity analysis

Since the Jacobian matrix of the synthesized manipulator was derived symbolically, the singular configurations can be identified from rank condition

$$\text{rank}(\mathbf{J}) < 4 \tag{19}$$

which can be divided into two categories.

On one hand, the first kind of singularity occurs when the 6×4 Jacobian $\mathbf{J}_\theta$ is rank-deficient. In other words, the set of joint twists $\{\boldsymbol{\xi}_1', \boldsymbol{\xi}_2', \boldsymbol{\xi}_3', \boldsymbol{\xi}_4'\}$ is linearly dependent. The singularity condition can thus be readily derived as $\alpha_1 = \pm\pi/2$. In such cases, the central shaft of the end-effector is collinear with the fixed axes of the active U-joints, as shown in Fig. 8(a). Then, the whole limb plane can rotate about this axis, without changing the direction of the central shaft. Under these conditions the manipulator losses partially its orientation capability. Moreover, in the case $\alpha_2 = \pm\pi/2$, the two limb planes coincide, as shown in Fig. 8(b). Thus, their intersection cannot be uniquely determined according to α_1 and α_2 neither the direction of the central shaft. As a consequence, the end-effector is capable of self-motion, even when all the actuators are locked. In such a kind of singularity, the entries a_{01}, a_{11}, or a_{12} is meaningless because of $\sin\phi = 0$ or $\boldsymbol{n}_2 \times \boldsymbol{n}_1 = \boldsymbol{0}$. Fortunately, these singular configurations are beyond the design workspace of the RCM manipulators, and hence, this issue is not investigated in this paper.

On the other hand, when $\overline{B_iD_i}$ becomes perpendicular to $\boldsymbol{u}$, as shown in Fig. 8(c), the manipulator finds itself at a singularity due to $l_{cd,i} = 0$. In this case, the motion direction of the slider is uncertain when the crank crosses this position. In addition, when the rocker is collinear with the coupler, as shown in Fig. 8(d), the slider reaches its limited position and cannot move forward.

Therefore, the dimension of the kinematic parameters, as well as the desirable workspace, should be carefully assigned for the synthesized manipulator to keep it away from these singular configurations. In the prototype, the kinematic parameters are mainly chosen to keep the angle between the coupler link and the central shaft in a range of small values within the workspace.

5. Experimental validation

5.1. Experimental setup

A physical prototype, displayed in Fig. 9, was produced to validate the feasibility of the synthesized manipulator. The decoupled two dof parallel wrist is employed to actuate the active U-joints in the planar URRH limbs. In this design, both servo motors are installed on the fixed base in a compact way. As a result, the rotations of the two axes of the U-joint can be independently controlled by the two motors through a capstan-cable mechanism and a slider-crank linkage. On the limb distal end, the concept of virtual screw was introduced to realize the differential motion of the coupled dual H-joint. Accordingly, the axial translation and rotation about the central shaft of the end-effector can be achieved via a cable-driven mechanism. Therefore, the 3R1T motion of the manipulator can be achieved by means of the inputs of the four DC motors mounted on the fixed base.

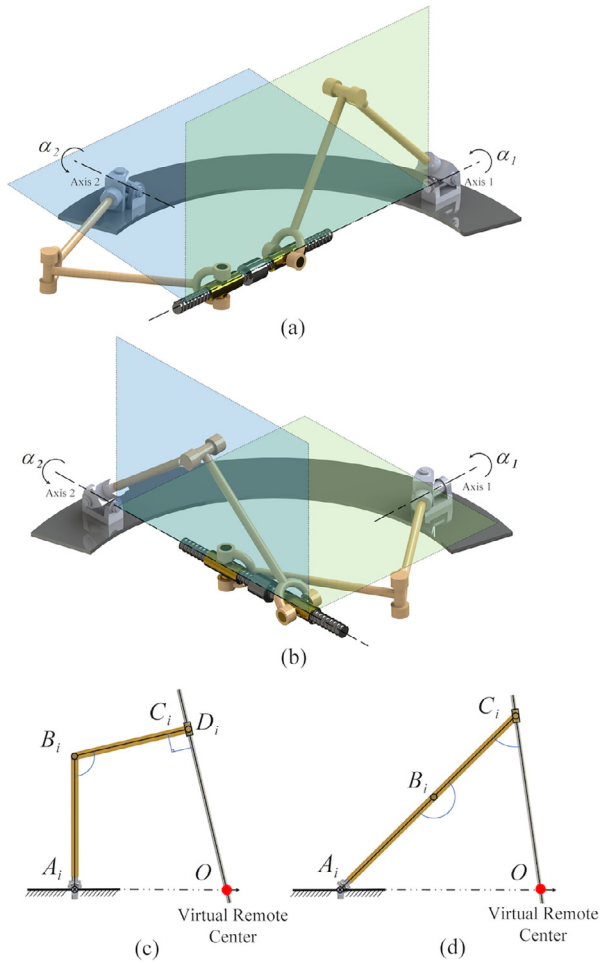

Fig. 8. Singularities of the proposed parallel RCM manipulator.

Table 1
Linkage length of two limbs.

limb	l_{oa}	l_{ab}	l_{bc}	l_{ae}	l_{ef}
1	130.0 mm	90.0 mm	83.4 mm	161.3 mm	161.3 mm
2	148.2 mm	85.0 mm	89.8 mm	161.3 mm	160.3 mm

The dimension of the kinematic parameters of the prototype are listed in Table 1. Note that the two limbs are arranged up and down at the distal end, the dimensions of the corresponding planar linkages being sightly different from each other to accommodate their ranges of motion. It is known that the pitch of virtual screw depends on the size of the pulley wheel whose radius is also given in Table 1. It is noteworthy that these kinematic parameters have been calibrated according to the collected configurations in the experiments.

As shown in Fig. 9, the multi-camera motion capture system OptiTrack is used to estimate the end-effector pose of the parallel manipulator. Four spherically mounted reflectors (SMRs), denoted R_0, R_1, R_2, and R_3, are attached to the central shaft to construct the tool frame {T} for the end-effector. As shown in the figure, R_0 and R_1 lie on the central shaft, whose connecting line corresponds to the $\boldsymbol{z}$-axis of {T}. Meanwhile, the line that connecting R_2 and R_3 relates to the $\boldsymbol{x}$-axis, whose intersection with the $\boldsymbol{z}$-axis is defined as the origin of {T}. Then, the $\boldsymbol{y}$-axis can be identified according to the right-hand rule.

In addition, two extra SMRs, R_4 and R_5, are attached to the capstan wheels of the active fixed axes of U-joints. The direction and the position of these fixed shafts, namely $\boldsymbol{u}_1$ and $\boldsymbol{u}_2$, can then be identified according to the circular trajectories of R_4 and R_5 as the manipulator moves. Accordingly, the system spatial frame {S} can be placed at the intersection point O and with its coordinate axes coincident with $\boldsymbol{u}_1$, $\boldsymbol{u}_2$, and $\boldsymbol{u}_0$, respectively. It should be noted that, in the physical prototype these two axes do not intersect at right angles exactly. Thus, the mid-point of their common perpendicular is selected as

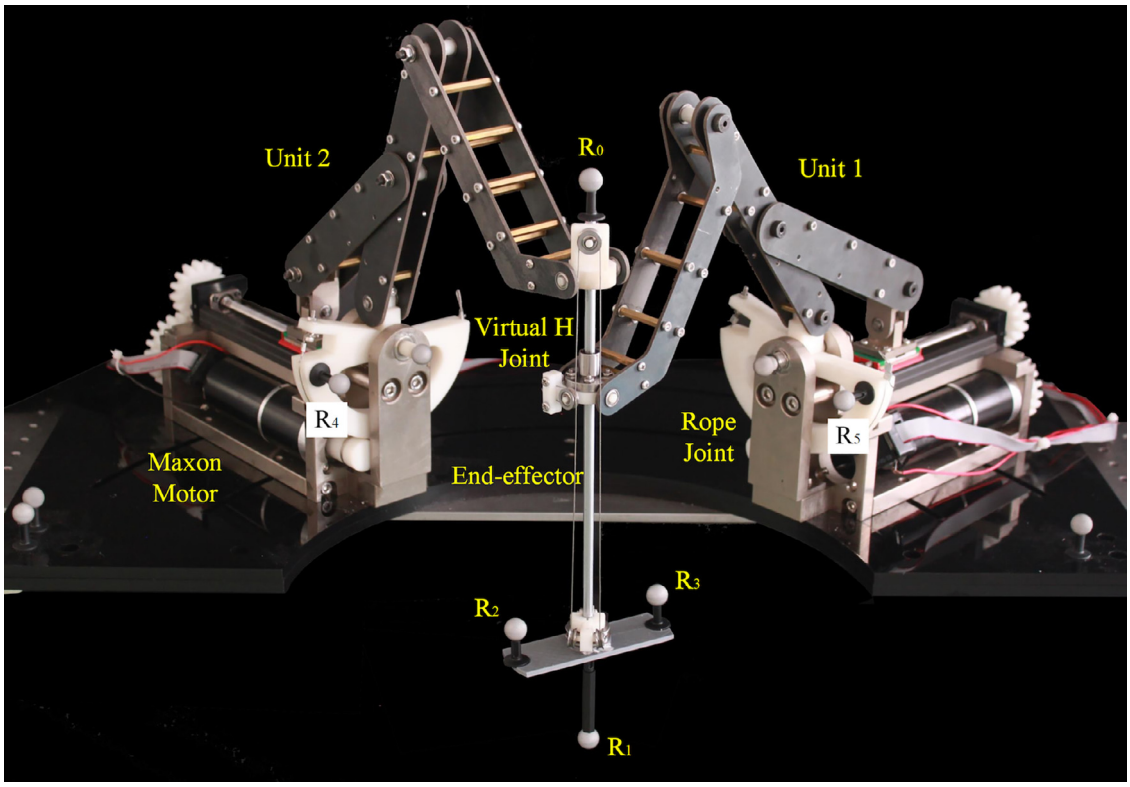

Fig. 9. Prototype of the synthesized parallel RCM manipulator.

the origin O and the corresponding direction is chosen as the $\boldsymbol{z}$-axis. The $\boldsymbol{x}$-axis is still set parallel to $\boldsymbol{u}_1$. Consequently, the direction of $\boldsymbol{y}$-axis is slightly different from $\boldsymbol{u}_2$.

In the experiments, all the datua estimated by the OptiTrack system have been transformed to frame {S}. Thus, the end-effector pose of the manipulator can be expressed as the homogeneous transformation matrix of {T} with respect to {S}. Since the central shaft of the end-effector is coincident with the $\boldsymbol{z}$-axis of {T}, the RCM characteristics are readily revealed in light of its trajectory.

5.2. Verification of the workspace and RCM characteristics

In this section, the workspace of the prototype is verified upon passing the central shaft through a bundle of radial lines concurrent at the RCM point. Based on these configurations, the RCM characteristics are also inspected via the position and orientation errors of the end-effector.

First, a range of 60° ($-30^\circ \sim 30^\circ$) angular input is assigned to the fixed axes of the U-joints in the limbs. For each axis, the range of rotation is discretized by 5°, which results in 169 (a 13×13 array) radial orientation for the central shaft. As shown in Fig. 10(a), the corresponding workspace is in the shape of a right rectangular pyramid with a 60° vertex angle. It should be noted that only the rotations of the first axes of the U-joints are taken into account to generate the pyramid workspace, with the corresponding radial lines normalized to a unit length.

This workspace is large enough for the MIS. However, there is not a standard workspace requirements for robot-assisted MIS. We thus assess the workspace upon comparison with that of the human surgeon. At present, the most popular minimally invasive surgeries include minimally invasive thoracic surgery [38], minimally invasive abdominal surgery [39] and minimally invasive knee surgery [40]. Among these kinds, the minimally invasive abdominal surgery requires the biggest workspace. Thus, we compared the workspace of the proposed manipulator with the human surgeon's. As shown in the Fig. 11, for a normal male, the length from neck to waist lies between 600–650 mm, of which the abdominal surgery occupies 1/2 approximately, the corresponding thickness being about 200–250 mm. Thus, the workspace, which is part of cone with 300 mm base-diameter and 200 mm height can satisfy the requirement of minimally invasive abdominal surgery.

From Fig. 10(a), it can be seen that the developed prototype can reach the prescribed workspace, which is large enough for minimally invasive surgery. However, the workspace of axial translation and rotation about the central shaft is too complex to illustrate for every reachable posture. Nevertheless, the radius of the pulley wheel in the distal differential mechanism, namely the pitch of the virtual screw, is relatively small when compared with the motion ranges of the sliders in the limbs' planar four-bar linkages. Thus, the central shaft can achieve full-cycle rotation at any posture of the manipulator's

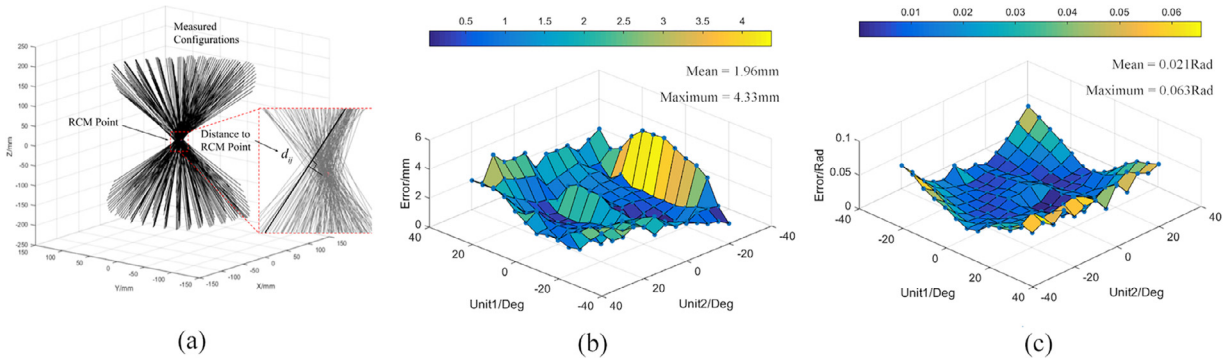

Fig. 10. Experimental validation of RCM property of the developed 3R1T RCM prototype.

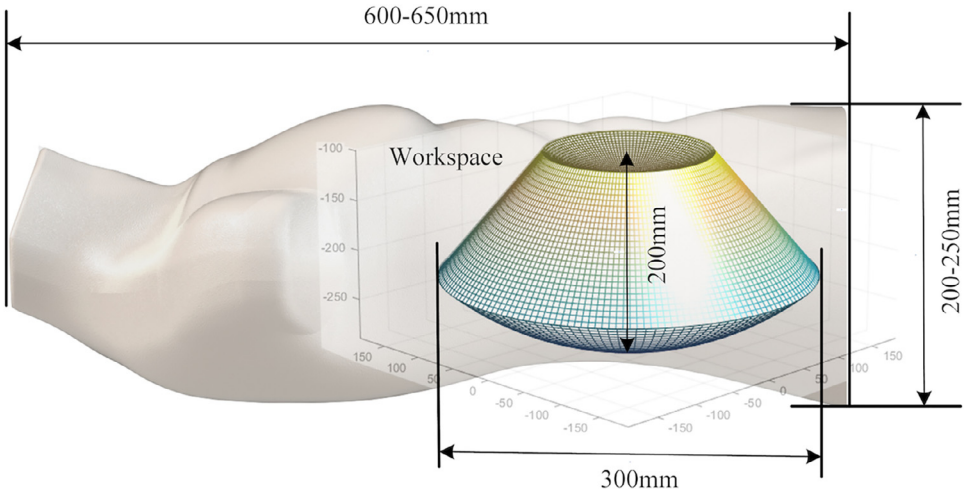

Fig. 11. Workspace analysis of the synthesized parallel RCM manipulator.

end-effector. The axial translation of the central shaft is realized by the synchronous motion of the planar limb linkages whose dimension can be particularly assigned according to a specific requirement.

Based on the collected postures, the RCM characteristics of the manipulator are verified by means of the concurrency of the radial orientations of the end-effector central shaft. Due to manufacturing/assembling errors, the central shaft of the prototype end-effector will not perfectly pass through the nominal stationary RCM point. Here, the actual point of concurrency is identified as the one that has the least distance to all these 169 lines, as shown in Fig. 10(a). The error distribution is obtained to evaluate the accuracy of the manipulator RCM characteristics.

Fig. 10(b) illustrates the distance errors of the central shaft from the specified RCM point at all collected postures. The mean and maximal magnitudes of these errors are 1.96 mm and 4.33 mm, respectively. This is acceptable in light of the size of the end-effector with a diameter of 6 mm for the central shaft. Meanwhile, the angular errors of the collected postures from their nominal values, as shown in Fig. 10(c), are also calculated as another precision assessment. From the figure, it is apparent that the mean and the maximal values of the orientation errors are 0.021 rad and 0.063 rad, respectively. This result is quite acceptable in light of the gearbox backlash of the servo motors and the transmission uncertainty of the capstan cable mechanisms. It is believed that the RCM characteristics of the synthesized manipulator can be further improved when more precise prototyping techniques are used.

5.3. Accuracy assessment

As reported in the above section, the misalignment of the end-effector central shaft was estimated to verify the RCM characteristics of the prototype. In this section, the translational and rotational errors about the axis of the virtual screw are studied to assess the accuracy of the differential motion mechanism. Meanwhile, the precision when follows a given trajectory is also tested to qualify the proposed manipulator for continuous operations.

As shown in Fig. 12, five orientations symmetric about the home position are selected for the end-effector to verify the translational and rotational accuracy about its central shaft. For each posture, four translational and four rotational displace-

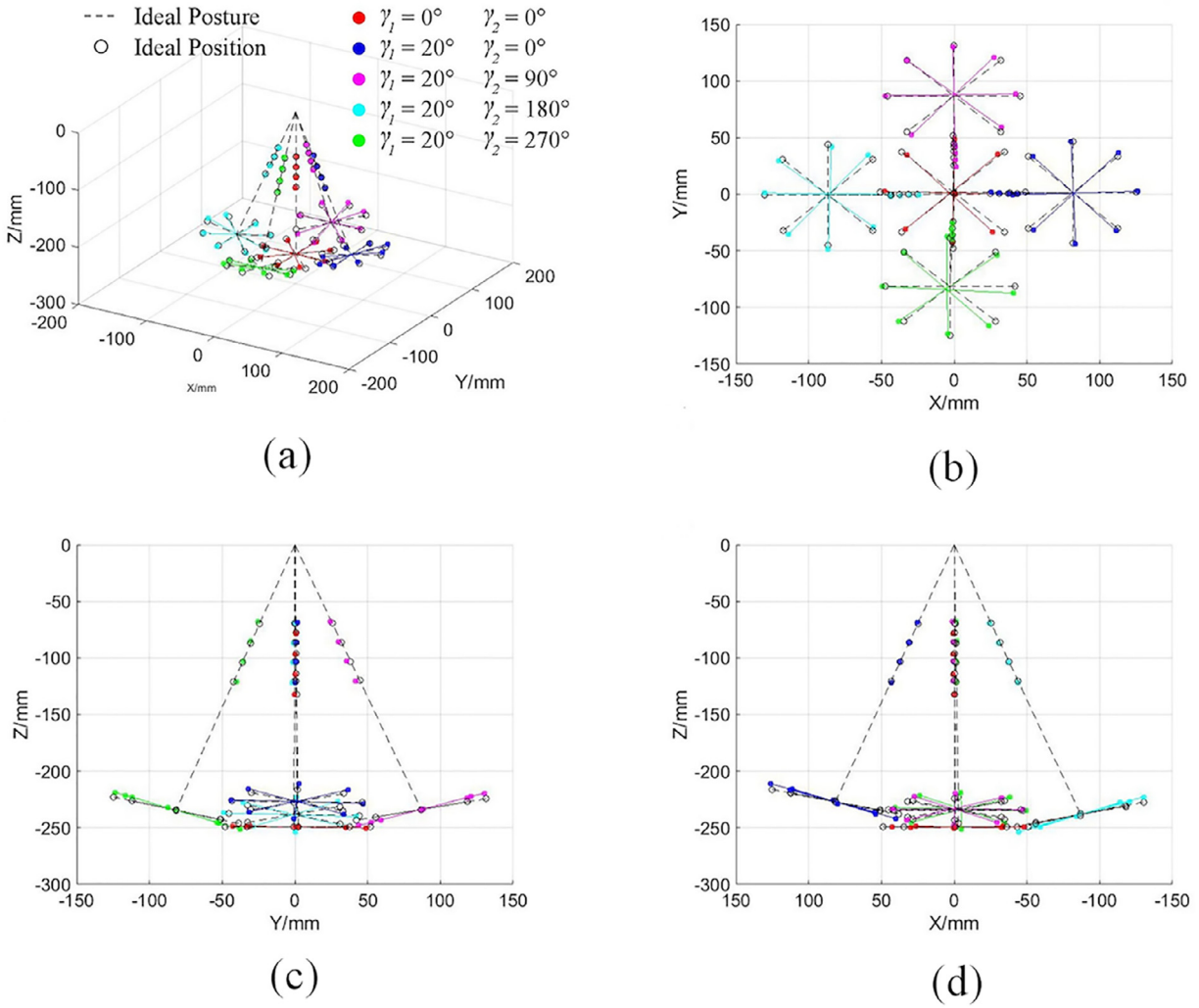

Fig. 12. Accuracy analysis of the developed 3R1T RCM prototype.

Table 2
Linear and angular errors of differential motion.

Error	Displ.	#0	#1	#2	#3	#4
linear	100 mm	1.21	1.76	2.23	1.02	2.11
(mm)	120 mm	1.35	0.68	2.34	1.48	1.84
	140 mm	1.61	0.42	2.39	1.24	1.21
	160 mm	1.31	1.31	2.46	2.03	2.06
Angular	0°	0.073	0.043	0.081	0.110	0.105
(rad)	45°	0.024	0.107	0.146	0.118	0.076
	90°	0.021	0.085	0.019	0.103	0.072
	135°	0.027	0.081	0.113	0.033	0.096

ments were specified to evaluate the differential motion of the cable-driven virtual screw mechanism. More specifically, d is set to 100 mm, 120 mm, 140 mm, and 160 mm, while γ sets to 0°, 45°, 90°, and 135°, respectively.

The results are given in Table 2. Each column corresponds to a specific direction of the central shaft, on the basis of which translational and rotational errors of four axial translational and other four axial rotational displacements are measured. From the results, it is shown the two kinds of errors induced by the differential motion of the virtual screw mechanism lie in an acceptable range for the prototype. The mean and maximal values of the linear errors are 1.43 mm and 2.46 mm, respectively, those for the angular errors being 0.077 rad and 0.146 rad, respectively.

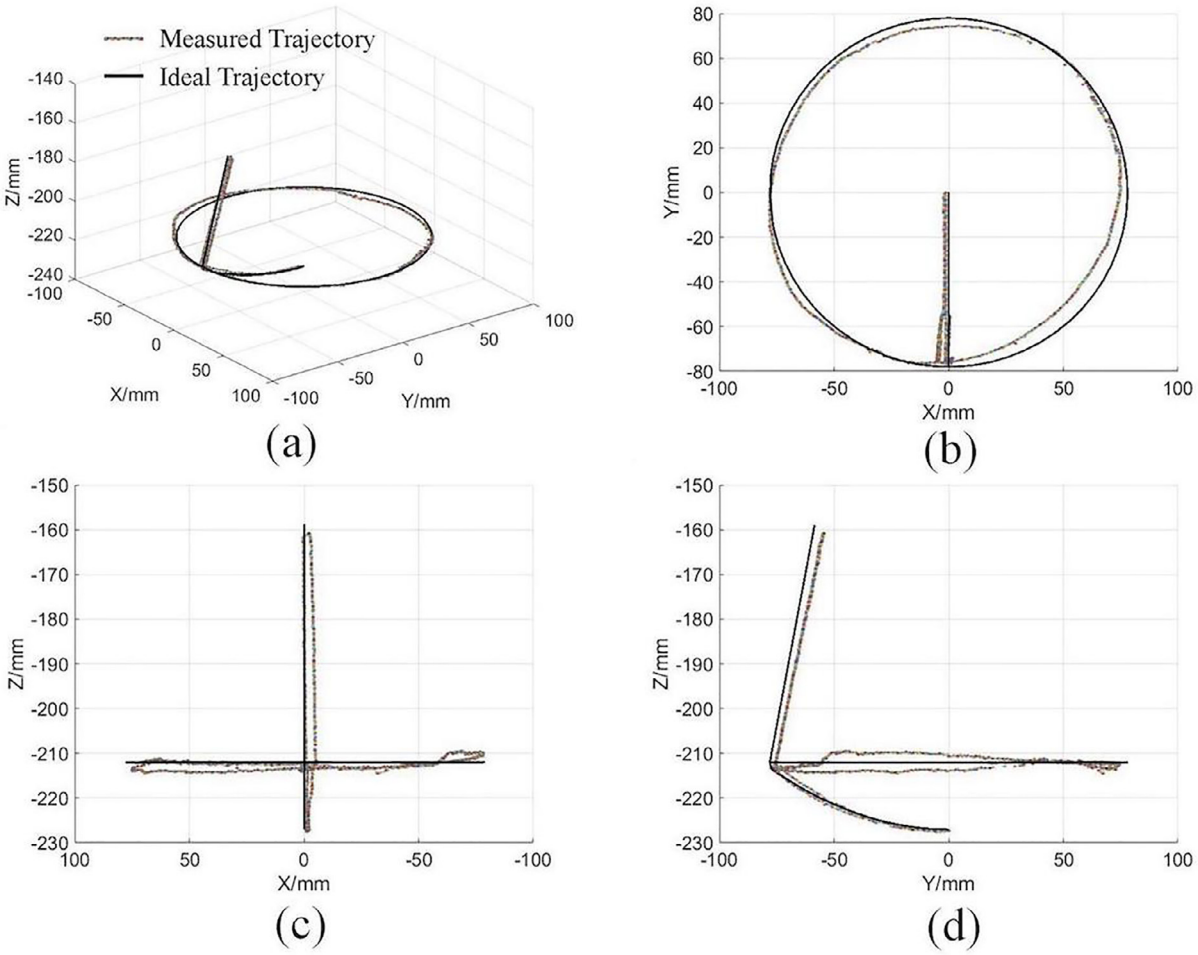

Fig. 13. Path-following capability of the developed 3R1T RCM prototype.

In addition, the prototype capability to precisely follow a given path is also studied in this work. As shown in Fig. 13, a compound trajectory, which consecutively combines pure translation, conic sweeping, and circular swaying, is prescribed for the central shaft of the manipulator end-effector. The path generated by the origin of the tool frame is illustrated in Fig. 13, in which the corresponding ideal path is also drawn for comparison. The results show that the prototype can perform typical motions of spatial RCM characteristics. Moreoverm the accuracy is higher than that obtained in previous experiments. This is because the influence of backlash on the positioning accuracy of the manipulator is less significant in continuous motions than at discrete configurations.

6. Conclusions

In this paper, a novel two-limb parallel manipulator, with 3R1T spatial RCM characteristics, is synthesized. A decoupled two dof parallel wrist is introduced to actuate the active universal joint in each limb, which makes the proposed four dof manipulator fully-parallel architecture. The concept of the virtual screw is also borrowed to generate cylindrical motion of the end-effector through a cable-driven differential mechanism. Due to its simple architecture, both the forward and inverse kinematics, as well as the Jacobian matrix, can be derived in closed-form. The four dof end-effector motion of the synthesized manipulator is partially decoupled, which eases its control. To verify the feasibility of the proposed design, a prototype was produced by means of simple fabrication techniques, on which preliminary experiments have been conducted. The results show that the proposed manipulator is capable of performing 3R1T RCM operations within a significantly large workspace. The positioning accuracy of the prototype is in an acceptable range in light of the adopted fabrication materials and techniques. Hence, it is believed that, because of its particular structure, the synthesized 3R1T parallel RCM manipulator has potential applications in robot-assisted minimally invasive surgery.

Declaration of Competing Interest

The authors declare that they have no known competing financial interests or personal relationships that could have appeared to influence the work reported in this paper.

Acknowledgment

This research work was supported in part by the National Key Research and Development program of China under the Grant No. 2017YFE0111300 and the National Natural Science Foundation of China under the Grant No. 51875334.

Supplementary material

Supplementary material associated with this article can be found, in the online version, at doi:10.1016/j.mechmachtheory.2020.103807.

References

[1] R. Isaacs, V. Podichetty, P. Santiago, F. Sandhu, J. Spears, K. Kelly, L. Rice, R. Fessler, Minimally invasive microendoscopy-assisted transforaminal lumbar interbody fusion with instrumentation, J. Neurosurg. 3 (2) (2005) 98–105.
[2] E. Rahimy, J. Wilson, T. Tsao, S. Schwartz, J. Hubschman, Robot-assisted intraocular surgery: development of the IRISS and feasibility studies in an animal model, Eye 27 (8) (2013) 972–978.
[3] S. Elayaperumal, M. Cutkosky, P. Renaud, B. Daniel, A passive parallel master-slave mechanism for magnetic resonance imaging-guided interventions, J. Med. Device. 9 (1) (2015) 11008.
[4] C. Kuo, J. Dai, Robotics for Minimally Invasive Surgery: A Historical Review from the Perspective of Kinematics, Springer Netherlands, pp. 337–354.
[5] G.S. Guthart, J.K. Salisbury, The intuitive/sup TM/telesurgery system: overview and application, in: Proceedings 2000 ICRA. Millennium Conference. IEEE International Conference on Robotics and Automation. Symposia Proceedings (Cat. No. 00CH37065), vol. 1, IEEE, 2000, pp. 618–621.
[6] G. Hamlin, A. Sanderson, A novel concentric multilink spherical joint with parallel robotics applications, in: Proceedings of the 1994 IEEE International Conference on Robotics and Automation, 1994, pp. 1267–1272.
[7] R. Taylor, J. Funda, D. Grossman, J. Karidis, D. LaRose, Remote center-of-motion robot for surgery, 1995.
[8] R. Taylor, J. Funda, B. Eldridge, S. Gomory, K. Gruben, D. LaRose, M. Talamini, L. Kavoussi, J. Anderson, A telerobotic assistant for laparoscopic surgery, IEEE Eng. Med. Biol. Mag. 14 (3) (1995) 279–288.
[9] J. Li, G. Zhang, Y. Xing, H. Liu, S. Wang, A class of 2-degree-of-freedom planar remote center-of-motion mechanisms based on virtual parallelograms, J. Mech. Rob. 6 (3) (2014) 31014.
[10] K. Kong, J. Li, H. Zhang, J. Li, S. Wang, Kinematic design of a generalized double parallelogram based remote center-of-motion mechanism for minimally invasive surgical robot, J. Med. Device. 10 (4) (2016) 41006.
[11] F. Zhang, X. Zhang, L. Hang, C. Lu, T. Furukawa, Type synthesis of n-parallelogram-based surgical arm with remote actuated configuration, in: X. Zhang, N. Wang, Y. Huang (Eds.), Mechanism and Machine Science, Springer Singapore, 2017, pp. 183–194.
[12] A. Gijbels, N. Wouters, P. Stalmans, H. VanBrussel, D. Reynaerts, E. VanderPoorten, Design and realisation of a novel robotic manipulator for retinal surgery, in: 2013 IEEE/RSJ International Conference on Intelligent Robots and Systems, 2013, pp. 3598–3603.
[13] S. Nisar, T. Endo, F. Matsuno, Design and kinematic optimization of a two degrees-of-freedom planar remote center of motion mechanism for minimally invasive surgery manipulators, J. Mech. Rob. 9 (3) (2017) 31013.
[14] G. Chen, J. Wang, H. Wang, A new type of planar 2-DOF remote center-of-motion mechanism inspired by the Peaucellier-Lipkin straight-line linkage, J. Mech. Des. 141 (1) (2019) 15001.
[15] R. Baumann, W. Maeder, D. Glauser, R. Clavel, The pantoscope: a spherical remote-center-of-motion parallel manipulator for force reflection, in: Proceedings of International Conference on Robotics and Automation, vol. 1, 1997, pp. 718–723.
[16] G. Li, T. Essomba, C. Wu, S. Lee, C. Kuo, Kinematic design and optimization of a novel dual-orthogonal remote center-of-motion mechanism for craniotomy, Proc. Inst. Mech.Eng. 231 (6) (2017) 1129–1145.
[17] M. Hadavand, M. Naish, R. Patel, A parallel remote center of motion mechanism for needle-based medical interventions, in: the 5th IEEE International Conference on Biomedical Robotics and Biomechatronics, 2014, pp. 1–6.
[18] G. Zong, X. Pei, J. Yu, S. Bi, Classification and type synthesis of 1-DOF remote center of motion mechanisms, Mech. Mach. Theory 43 (12) (2008) 1585–1595.
[19] Y. He, P. Zhang, H. Jin, Y. Hu, J. Zhang, Type synthesis for remote center of motion mechanisms based on coupled motion of two degrees-of-freedom, J. Mech. Des. 138 (12) (2016) 122301.
[20] E. Hempel, H. Fischer, L. Gumb, T. Hohn, H. Krause, U. Voges, H. Breitwieser, B. Gutmann, J. Durke, M. Bock, A. Melzer, An MRI-compatible surgical robot for precise radiological interventions, Comput. Aided Surg. 8 (4) (2003) 180–191.
[21] S. Liu, L. Harewood, B. Chen, C. Chen, A skeletal prototype of surgical arm based on dual-triangular mechanism, J. Mech. Rob. 8 (4) (2016) 41015.
[22] S. Liu, B. Chen, S. Caro, S. Briot, L. Harewood, C. Chen, A cable linkage with remote centre of motion, Mech. Mach. Theory 105 (2016) 583–605.
[23] J. Li, G. Zhang, A. Müller, S. Wang, A family of remote center of motion mechanisms based on intersecting motion planes, J. Mech. Des. 135 (9) (2013) 91009.
[24] T. Tanev, Minimally-invasive-surgery parallel robot with non-identical limbs, in: the 10th IEEE/ASME International Conference on Mechatronic and Embedded Systems and Applications, 2014, pp. 1–6.
[25] C. Kuo, J. Dai, Kinematics of a fully-decoupled remote center-of-motion parallel manipulator for minimally invasive surgery, J. Med. Device 6 (2) (2012) 21008.
[26] R. Beira, L. SantosCarreras, G. Rognini, H. Bleuler, R. Clavel, Dionis: a novel remote-center-of-motion parallel manipulator for minimally invasive surgery, Appl. Bionics Biomech. 8 (2) (2011) 191–208.
[27] M. Zoppi, D. Zlatanov, C. Gosselin, Analytical kinematics models and special geometries of a class of 4-DOF parallel mechanisms, IEEE Trans. Rob. 21 (6) (2005) 1046–1055.
[28] Q. Li, J.M. Hervé, P. Huang, Type synthesis of a special family of remote center-of-motion parallel manipulators with fixed linear actuators for minimally invasive surgery, J. Mech. Rob. 9 (3) (2017) 31012.
[29] L. Bedem, Realization of a Demonstrator Slave for Robotic Minimally Invasive Surgery, Technische Universiteit Eindhoven, 2010 Ph.D. thesis.
[30] Z. Li, Y. Lou, Y. Zhang, B. Liao, Z. Li, Type synthesis, kinematic analysis, and optimal design of a novel class of Schönflies-motion parallel manipulators, IEEE Trans. Autom. Sci. Eng. 10 (3) (2012) 674–686.
[31] T. Harada, J. Angeles, Kinematics and singularity analysis of a CRRHHRRC parallel Schönflies motion generator, Trans. Can. Soc. Mech.Eng. 38 (2) (2014) 173–183.

[32] P. Lee, J. Lee, C. Lee, Four novel pick-and-place isoconstrained manipulators and their inverse kinematics, in: 2010 ASME International Design Engineering Technical Conferences and Computers and Information in Engineering Conference, 2010, pp. 1079–1088.
[33] P.K. Eskandary, J. Angeles, The translating π-joint: design and applications, Mech. Mach. Theory 122 (2018) 361–370.
[34] C. Chen, Mobility analysis of parallel manipulators and pattern of transform matrix, J. Mech. Rob. 2 (4) (2010) 41003.
[35] M. Carricato, V. Parenti-Castelli, A novel fully decoupled two degrees-of-freedom parallel wrist, Int. J. Rob. Res. 23 (6) (2004) 661–667.
[36] P. Eskandary, J. Angeles, The virtual screw: concept, design and applications, Mech. Mach. Theory 128 (2018) 349–358.
[37] X. Kong, C. Gosselin, Type Synthesis of Parallel Mechanisms, Springer Berlin Heidelberg, 2007.
[38] A.D. Sihoe, The evolution of minimally invasive thoracic surgery: implications for the practice of uniportal thoracoscopic surgery, J. Thorac. Dis. 6 (Suppl 6) (2014) S604.
[39] A.G. Harrell, B.T. Heniford, Minimally invasive abdominal surgery: lux et veritas past, present, and future, Am J. Surg. 190 (2) (2005) 239–243.
[40] R.S. Laskin, Minimally invasive total knee arthroplasty: the results justify its use, Clin. Orthop. Relat.Res.® 440 (2005) 54–59.